

High-order harmonics from backscattering of delocalized electronsChuan Yu , Ulf Saalmann , and Jan M. Rost *Max-Planck-Institut für Physik komplexer Systeme, Nöthnitzer Straße 38, 01187 Dresden, Germany* (Received 26 February 2021; revised 30 April 2021; accepted 14 March 2022; published 11 April 2022)

It is shown that electron backscattering can enhance high-order-harmonic generation in periodic systems with broken translational symmetry. Paradigmatically, we derive for a finite chain of atoms the harmonic cutoff due to electrons backscattered from the edges of the chain and demonstrate a maximum in the harmonic yield if twice the quiver amplitude of the driven electrons equals the chain length. For an intuitive understanding of our quantum results we develop a refined semiclassical trajectory model with finite electron-hole separation after tunneling. We demonstrate that the same “tunnel exit” also holds for interband harmonics in conventional periodic solid-state systems.

DOI: [10.1103/PhysRevA.105.L041101](https://doi.org/10.1103/PhysRevA.105.L041101)

Since the pioneering experiment by Ghimire *et al.* [1] high-order-harmonic generation (HHG) with strong laser fields applied to solids has been a focus of experimental and theoretical research with first reviews available [2–4]. The so-called three-step model [5] is key to understand the microscopic electron dynamics of HHG in atoms and molecules semiclassically in terms of classical trajectories [6]. It has been adapted successfully for interband HHG in solids [7–9], suggesting that fundamental properties of high-order harmonics are ruled by the same basic principles from atoms to solids. On the other hand, a solid-state environment should offer more possibilities to influence these phenomena than an atom due to the larger structural complexity and variability [10–14]. Indeed, under suitable conditions, a solid-state HHG spectrum exhibits several cutoffs [10,15] due to the (band-)structured continuum of electrons, in contrast to the single atomic cutoff.

In an atomic context, cutoffs can be extended if the laser-driven electron acquires a larger momentum through backscattering from another atom or ion. This requires a large distance of the order of the atomic quiver amplitude A_0/ω_0 between the backscattering and recombining ion, where A_0 is the peak vector potential and ω_0 is the carrier frequency of the laser. This can theoretically be achieved in laser-assisted ion-atom collisions with a suitable impact parameter [16] or for above-threshold ionization in rare-gas clusters with a suitable size, as demonstrated recently in an experiment [17], but not in molecules which are typically too small. Solid-like systems, on the other hand, can easily match the spatial requirements set by the quiver amplitude of conduction-band electrons and any irregularity in their periodicity may give

rise to backscattering. Indeed, we will analytically predict and numerically demonstrate in the following significantly extended HHG cutoffs through backscattering.

This Letter reveals a backscattering mechanism of delocalized electrons in a solid-state context. Yet, as in the familiar case of elastic backscattering of localized electrons from a nucleus in atoms or molecules, this mechanism is characterized by a reversal of the electron momentum $k \rightarrow -k$. To be specific, we study backscattering for a finite chain of regularly placed atoms, where the global potential causes backscattering of the delocalized electron wave packet near the end of the chain with the driving laser field polarized along the chain. This phenomenon should not be confused with backscattering of localized electrons between two layers of a bilayer material with laser polarization perpendicular to the layer planes [18].

We will show that extended cutoffs through backscattering from the edge can occur and that HHG is most efficient if the full excursion of the excited laser-driven electron (twice the quiver amplitude x_q) matches the length of the chain, i.e., if the number of atoms $N \approx N_q$ with the latter defined by $2x_q \equiv N_q d$ and d denoting the interatomic distance. Motivated by simple scaling arguments and the (semi)classical trajectory picture for interband harmonics, the predicted cutoff and maximal high-order-harmonic yield are accurately reflected in the HHG spectra obtained from the laser-driven current. Atomic units (a.u.) are used throughout unless stated otherwise.

To keep the situation as simple as possible, we investigate HHG from a chain of N atoms with a lattice constant (interatomic distance) of $d = 7$ a.u. and four active electrons per atom, as introduced before [19]. Apart from small modifications we find the electron dynamics in a chain with $N \gtrsim 10$ well described with the band structure of the periodic system (see Supplemental Material [20]). This is consistent with earlier work [21], in which the HHG response from a finite chain was found to deviate from that of single atoms or small molecules, revealing a solidlike behavior at rather small system sizes.

Published by the American Physical Society under the terms of the Creative Commons Attribution 4.0 International license. Further distribution of this work must maintain attribution to the author(s) and the published article's title, journal citation, and DOI. Open access publication funded by the Max Planck Society.

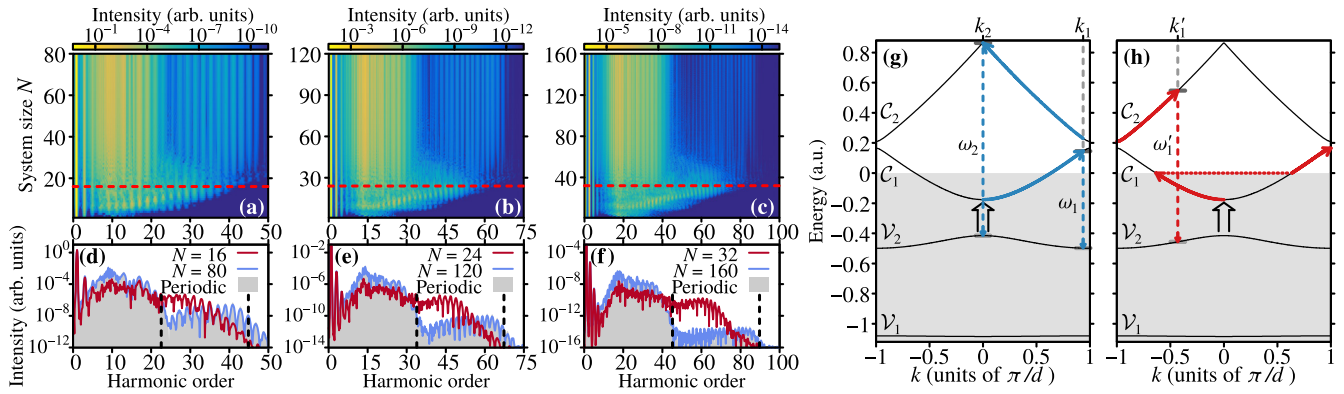


FIG. 1. HHG spectra as a function of harmonic order and system size N for wavelengths of 1600 nm (a), 2400 nm (b), and 3200 nm (c) and for the same wavelengths but at fixed $N = 16$ (d), $N = 24$ (e), and $N = 32$ (f), indicated by horizontal dashed lines in panels (a)–(c). The spectra of the periodic system are shown as shaded area for comparison. The dashed lines indicate the estimates of the first and second cutoff for the periodic system at ω_1 and ω_2 , specified in the text. (g) Sketch of the k -space dynamics in the periodic system, for an electron excited to the bottom of \mathcal{C}_1 at $A(t_0) \approx -A_0$. The maximal \mathcal{C}_1 - \mathcal{V}_2 and \mathcal{C}_2 - \mathcal{V}_2 band energy differences (i.e., the cutoffs ω_1 and ω_2) are achieved at $k_1 = 2A_0$ and $k_2 = 0$. (h) Sketch of the k -space dynamics in the finite system, with an edge backscattering event in \mathcal{C}_1 at the vacuum level occurring at $A(t_s) = -A_0$. The horizontal dotted line represents the sign change of $k(t)$ due to backscattering. With a subsequent band-gap transition to \mathcal{C}_2 , this sketch corresponds to the maximally achievable harmonic energy in the backscattering case ω'_1 at k'_1 (see text).

For the chain of N atoms we compute the harmonic spectrum generated per atom:

$$S_N(\omega) \propto N^{-2} \left| \int dt J_{\text{tot}}(t) W(t) \exp(-i\omega t) \right|^2, \quad (1)$$

where $J_{\text{tot}}(t)$ is the total current in the system and $W(t)$ is a window function of the laser-pulse-envelope shape for improving the signal-to-noise ratio. Details of the methods and parameters used as well as the periodic treatment for the limit $N \rightarrow \infty$ can be found elsewhere [22]. The finite chains are treated with density-functional theory (DFT) on a real-space grid much larger than the system extension Nd without using periodic boundary conditions; in this way we construct effective (multiwell) potentials with edges self-consistently, and also account for the escape of laser-driven electrons from the system as in a realistic situation [19]. The laser pulse with frequency ω_0 is described in dipole approximation by a vector potential $A(t) = A_0 \sin^2[\omega_0 t / (2n_{\text{cyc}})] \sin(\omega_0 t)$ for $0 \leq t \leq 2\pi n_{\text{cyc}} / \omega_0$ and $A(t) = 0$ otherwise. All presented results are obtained with $n_{\text{cyc}} = 9$ and $A_0 = 0.21$, but backscattering is not restricted to specific laser parameters as will become clear.

An overview of the results is presented in Fig. 1 for the three laser wavelengths $\lambda = 1600, 2400,$ and 3200 nm. The vertical structure in Figs. 1(a)–1(c) for large N signals that the HHG spectra approach the periodic limit $N \rightarrow \infty$. However, in the lower central part of Figs. 1(a)–1(c) one sees a stronger HHG response which prevails for a certain range of systems sizes. To see this more clearly, Figs. 1(d)–1(f) show (in dark red lines) spectra at the system sizes $N = 16, 24,$ and 32 , where the HHG response for midsize harmonic orders is enhanced. These selected system sizes [marked by horizontal dashed lines in Figs. 1(a)–1(c)] have the widest enhancement region. The enhancement is particularly evident in comparison to the periodic limit (gray areas). The latter is apparently reached in the longest chains considered for each wavelength ($N = 80, 120,$ and 160 , respectively), which are presented in light blue lines. All the spectra in Figs. 1(d)–1(f) exhibit a sharp rise

of intensity when the harmonic energy goes above the \mathcal{C}_1 - \mathcal{V}_2 band gap. This indicates that the harmonics above this energy gap are dominated by interband processes, since such a close link between the emitted photon energy and the band energy difference is a clear signature of interband harmonics. As we will see below, the interband recombination picture indeed provides a good interpretation of the spectral shape as well as the time-frequency profile for the high-order harmonics.

The periodic spectra exhibit two clear steps corresponding to the end (cutoff) of a first and second plateau marked by dashed vertical lines. As one can see from the band structures in Fig. 1(g), these cutoffs represent the maximally possible recombination energies [15] with the valence band $\mathcal{V}_2(k)$: $\omega_1 = \mathcal{C}_1(k_1) - \mathcal{V}_2(k_1) = 0.64$ at $k_1 = 2A_0 = 0.94 \pi/d$ and $\omega_2 = \mathcal{C}_2(k_2) - \mathcal{V}_2(k_2) = 1.28$ at $k_2 = 0$. The large gaps to all other bands prevent \mathcal{V}_1 from actively participating in the HHG processes, as discussed before [19]. An electron, excited from the second valence band \mathcal{V}_2 at t_0 , preferentially enters the first conduction band \mathcal{C}_1 at $k_0 \approx 0$ near the Γ point ($k = 0$) and subsequently moves with momentum:

$$k(t) = A(t) - A(t_0) + k_0. \quad (2)$$

This time-dependent k -space motion always holds in the periodic limit, but can be modified by backscattering in finite systems, as will be discussed below.

The enhanced spectra [dark red lines in Figs. 1(d)–1(f)] exhibit a small dip at the first cutoff but the enhancement does not extend to the second cutoff. This observation suggests that the enhancement is not due to a more efficient mechanism to enter \mathcal{C}_2 preserving the original $k(t)$. Rather, it must be a process which changes $k(t)$. This can be achieved by elastic scattering in the presence of a laser field. Indeed, as we will see, the enhancement is due to electrons in \mathcal{C}_1 , being backscattered from the edge of the chain. To this end, we have to understand how elastic scattering in real space manifests itself in the band picture of reciprocal space.

When an electron wave packet approaches the system edge, it can either be reflected from it (i.e., being backscattered) or

leak out of the system (i.e., being ionized). Backscattering or ionization will be dominant if its mean energy is lower or higher, respectively, than the vacuum level. In the classical three-step description, backscattering of a laser-driven localized electron at a time t_s is assumed to be elastic, resulting in a sign change of the electron's instantaneous momentum. In a quasiperiodic system, the delocalized electron (and the accompanying hole) suffer the analogous momentum kick while moving on their respective band \mathcal{B} with dispersion $\mathcal{B}(k)$, i.e.,

$$k(t > t_s) = A(t) - 2A(t_s) + A(t_0) - k_0. \quad (3)$$

This is illustrated in Fig. 1(h) for the electron. Note that the reversal of the momentum indicated by the horizontal dotted line is an essential signature of elastic backscattering that is distinct from normal intraband motions such as dynamical Bloch oscillations [23] in which $k(t)$ does not jump. In general, the band energy at backscattering must be below the vacuum level $E = 0$ to avoid ionization. Therefore, the maximal momentum at backscattering is $k_s = 0.285$, defined by $\mathcal{C}_1(k_s) = 0$. Since the electron can acquire at most a momentum of $2A_0$ through (unperturbed) interaction with the laser field, the maximal final momentum is $k'_1 = k_s + 2A_0 - 2\pi/d$ in the first Brillouin zone (BZ) leading to the recombination energy $\omega'_1 = \mathcal{C}_2(k'_1) - \mathcal{V}_2(k'_1) = 1.0$ which defines the first cutoff energy extended through backscattering. Indeed, this corresponds to harmonic order 35, 53, and 70 for the wavelengths $\lambda = 1600, 2400$, and 3200 nm, respectively, where the yield of the enhanced spectra (dark red lines) in Figs. 1(d)–1(f) decreases.

In passing we note that, without backscattering, the electron in Fig. 1(h) would never have the chance to pass the BZ boundary and enter \mathcal{C}_2 via a subsequent band-gap transition. Hence, edge backscattering suggests itself as a pathway to high-energy states in analogy to backscattered electrons from an ion in the atomic context. There, however, backscattering only leads to higher photoelectron energies [17,24], but not to larger cutoffs in HHG. This is mainly due to the fact that the electron's wave function in the atomic context is usually spatially localized on the ion (playing the role of the hole) and the continuum electron wave packet. The lacking overlap prevents recombination necessary for HHG between the energetic electron far away from the ion available for recombination. In solidlike systems, on the other hand, we deal with spatially delocalized Bloch electrons, for which overlap of electron-hole wave functions can be more easily achieved [25]. Moreover, delocalized electrons reflected by the edges continue to move inside the system, allowing them to recombine with significant wave-function overlap. Therefore, backscattering represents a promising mechanism for increasing the energy of solid-state harmonics.

As a next step we work out which role the spatial extension of the chain plays for backscattering. To this end we vary in Fig. 2 the wavelength λ while keeping the vector potential amplitude A_0 fixed. The latter ensures that the dynamics in momentum space, and in particular the energy gain through backscattering depending on A_0 as discussed so far, remains the same while through the variation of the wavelength the quiver amplitude $x_q \propto A_0 \lambda$ changes linearly, resulting in different scales for the spatial dynamics. Hence, locking the

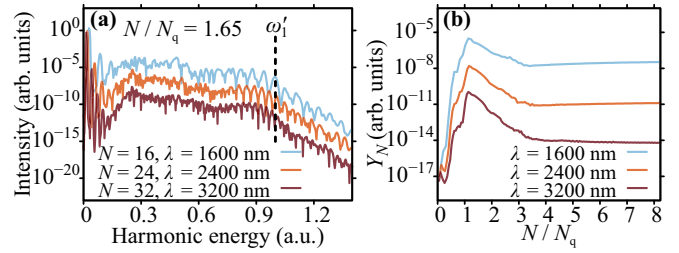


FIG. 2. The HHG spectra from Figs. 1(d)–1(f) as a function of photon energy (a) and their integrated yield Y_N beyond the first cutoff ω_1 as a function of scaled system size N/N_q (b). The vertical dashed line in panel (a) represents the edge-backscattering cutoff at $\omega'_1 = 1.0$, discussed in the text.

ratio of chain length versus wavelength N/λ in addition to an identical A_0 should provide similar conditions for the high-order-harmonic generating electron dynamics and we expect similar spectra, provided the HHG yield is shown as a function of harmonic energy, as done in Fig. 2(a). The similarity of the three spectra with the extended cutoff at $\omega'_1 = 1.0$ is evident.

In Fig. 2(b) we demonstrate that this similarity implies a universal ratio N_q/λ where the largest enhancement of the high-order-harmonic yield for edge backscattering occurs. For this purpose we integrate the yield in the spectral region of enhancement, $Y_N = \int_{\omega_1}^{\omega'_1} d\omega S_N(\omega)$. That the curves level off for large N simply reflects convergence to the periodic limit without edge backscattering. That all three integrated yields have a similar shape over the entire scaled range of N illustrates the universality of the underlying strong-field dynamics of delocalized electrons provided that momentum and spatial dynamics are equivalent. Most interesting in the context of backscattering is the sharp rise and maximum of Y_N which occur close to $N/N_q = 1$ for different wavelengths with the critical number of atoms $N_q = 2x_q/d$, where the length $N_q d$ of the chain equals the full quiver excursion $2x_q$ of the excited electron. This can be understood by considering the extreme cases: For $2x_q \ll Nd$ only a small fraction of excited electron density can reach the chain edge for backscattering. The limit $2x_q \gg Nd$ implies that $A(t_s)$ and $A(t_0)$ hardly differ and therefore the momentum gain at backscattering $\Delta k = -2k(t_s) = 2[A(t_0) - A(t_s)]$, with the band-gap tunneling assumption $k_0 = 0$, becomes negligible. Hence, $Nd = 2x_q$ is the optimal length where the entire spatially distributed excited electron density can participate in backscattering.

We note that while the momentum scale A_0 is a property of the light only this is not the case for the spatial scale x_q , the quiver amplitude, which depends also on the band structure. With $k(t)$ given by Eq. (2), the position-space motion of a Bloch electron in band \mathcal{B} reads

$$\Delta x_{\mathcal{B}}(t) \equiv x_{\mathcal{B}}(t) - x_{\mathcal{B}}(t_0) = \int_{t_0}^t dt' \frac{d}{dk} \mathcal{B}(k) \Big|_{k=k(t')}. \quad (4)$$

Within the Kane band approximation [26], an explicit expression for the quiver motion can be given which is even analytically solvable if the electron moves with initial condition $A(t_0) = 0$ in the conduction band [20]. In this case $x_q = [A_0/(m_* \omega_0)] \arctan(a)/a$, with $a = A_0/k_*$, where m_* is the effective mass of the electron and k_* is the band's momentum scale [27].

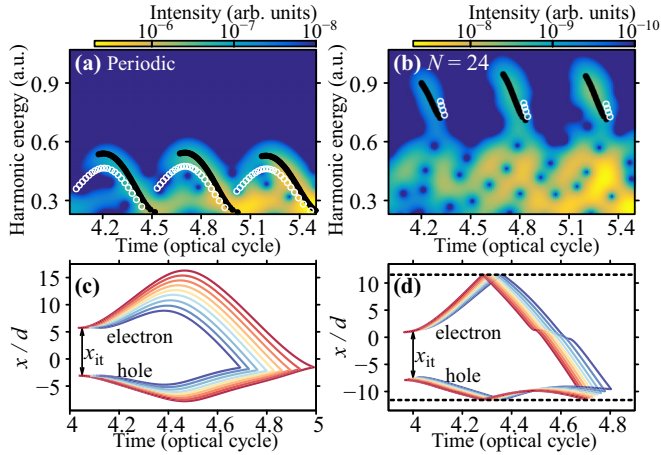


FIG. 3. HHG time-frequency profile at $\lambda = 2400$ nm for the periodic system (a) and a finite chain of $N = 24$ (b), respectively. The black dots are traces obtained from our refined semiclassical trajectories with finite electron-hole separation x_{it} after tunneling. Consistent with the Taylor expansion (see text) we use the same $x_{it} = -E_g/F(t_m)$ for all trajectories in the small interval $|t_0 - t_m| < 0.25\pi/\omega_0$ around $t_m = 3.5T, 4.0T, 4.5T$ contributing to the traces. The white circles are traces obtained from trajectories assuming $x_{it} = 0$ without complex initial time (see text). Panels (c) and (d) provide representative trajectories forming the black traces in panels (a) and (b) in real space. The horizontal dashed lines in panel (d) indicate the locations of the edge atoms, where backscattering is assumed to occur.

Finally, we discuss how the HHG time-frequency profile, shown in Fig. 3, obtained by Gabor transforming the quantum current in Eq. (1), can be mapped onto classical trajectories from Eq. (4) for electron-hole pairs. It is *a priori* unclear if the (quantum) reflection-based backscattering mechanism can be described adequately with trajectories. Certainly, such trajectories will require refined spatial properties. To identify them, we first analyze the (standard) periodic system case.

To fulfill the stationary-phase condition for the tunneling step $E_{C\mathcal{V}}[k(t_i)] \equiv \mathcal{C}_1[k(t_i)] - \mathcal{V}_2[k(t_i)] = 0$ justifying the trajectory picture in the first place [2], we propagate electron and hole trajectories from an initial complex time $t_i = t_0 + i\tau$ over an imaginary time span $i\tau$ realizing the tunneling process. Tunneling happens most likely near the band gap E_g at the Γ point ($k = 0$), where each band typically has an approximately parabolic dispersion around its local extremum. With an effective mass, we can write for small $|k|$ the difference in the band dispersion as $E_{C\mathcal{V}}(k) \approx E_g + k^2/(2\mu)$ with $\mu^{-1} \equiv \frac{d^2}{dk^2} E_{C\mathcal{V}}(k)|_{k=0}$. Hereby μ is the *reduced* effective mass of the electron-hole pair, which has for the system considered here the value $\mu = 0.108$.

Then we approximately solve $E_{C\mathcal{V}}[k(t_0 + i\tau)] = 0$ describing tunneling with complex time and momentum. The trajectories for interband HHG are typically created when the laser field $F(t) = -\frac{d}{dt}A(t)$ is near its extrema at times t_m fulfilling $\frac{d}{dt}F(t)|_{t=t_m} = 0$. This leads to a relatively small τ , for which we make a (truncated) Taylor expansion $A(t_0 + i\tau) \approx A(t_0) - i\tau F(t_0)$ and therefore $k(t_0 + i\tau) \approx -i\tau F(t_0)$. Hence, τ is approximately given by $\tau^2 = 2\mu E_g/F^2(t_0)$. Denoting

the electron-hole separation by $\Delta_{C\mathcal{V}}(t) \equiv x_C(t) - x_V(t)$, and integrating the trajectory from $t_0 + i\tau$ to t_0 along the imaginary-time axis leads to a “tunnel exit”:

$$\begin{aligned} x_{it} &\equiv \Delta_{C\mathcal{V}}(t_0) - \Delta_{C\mathcal{V}}(t_0 + i\tau) \\ &= \int_{t_0 + i\tau}^{t_0} dt' \frac{d}{dk} E_{C\mathcal{V}}[k(t')] \approx -F(t_0)\tau^2/2\mu \\ &= -E_g/F(t_0) \approx -E_g/F(t_m), \end{aligned} \quad (5)$$

which defines the separation of electron and hole trajectories when they start their dynamics at real time t_0 ($\approx t_m$) on the conduction and valence band, respectively.

Before tunneling at the complex time $t_0 + i\tau$, electron and hole are at the same position, i.e., $\Delta_{C\mathcal{V}}(t_0 + i\tau) = 0$. After tunneling in imaginary time, however, when the trajectory starts propagating in real time at t_0 , the electron-hole separation is $\Delta_{C\mathcal{V}}(t_0) = x_{it}$, approximated in Eq. (5). Accordingly, the recombination condition at time t_r is $\Delta_{C\mathcal{V}}(t_r) = \Delta_{C\mathcal{V}}(t_0 + i\tau) = \Delta_{C\mathcal{V}}(t_0) - x_{it} = 0$, which naturally defines the electron-hole recollisions as harmonic emission events. Note that in the standard solid-state trajectory model $x_{it} = 0$ is assumed [2,8]. In Fig. 3(a) one sees that the trajectories starting with $x_{it} = -E_g/F(t_m)$, shown in black dots, track the HHG profile much better than the ones with $x_{it} = 0$, shown in white circles, which have been used so far.

In the case of backscattering for a finite chain, trajectories with the same tunnel exit x_{it} propagate until the electron-hole separation reaches the chain length and if the energy of the electron is below the vacuum level, namely, $\mathcal{C}_1(t_s) < 0$, backscattering takes place by elastic reflection of the trajectories at the chain edges [horizontal dashed lines in Fig. 3(d)]. This means that for $t > t_s$ Eq. (3) holds instead of Eq. (2). These trajectories [black dots in Fig. 3(b)] trace the quite different HHG profile very well, while trajectories with $x_{it} = 0$ (white circles) disagree with the quantum profile. We may conclude that semiclassical trajectories that include initial propagation in imaginary time lead to a finite electron-hole separation x_{it} after tunneling, which should be taken instead of $x_{it} = 0$ for condensed-matter interband harmonics in a fully periodic system as well as for the new harmonics from backscattering in a finite chain.

To summarize, we have established backscattering of delocalized electrons as a mechanism to extend the cutoff for harmonics in quasiperiodic systems with an inherent length scale due to broken translational symmetry. For simplicity and consistency, we have chosen to demonstrate and analyze backscattering with finite chains of atoms solving the many-electron dynamics based on DFT. This has allowed us to link the quiver amplitude of the driven electron to the extension of the system, revealing that one achieves the highest integrated harmonic yield beyond the first cutoff of the fully periodic system, if twice the quiver amplitude is approximately equal to the length of the atomic chain. The band energy at the momentum where backscattering takes place must be below the vacuum level of the system, otherwise ionization outweighs reflection. This is a universal condition for the extended cutoff, which takes, however, different values depending on the band structure.

High-order harmonics due to backscattering can be described in terms of a simple trajectory picture with elastic

reflection from the edges of the atomic chain and a finite initial separation x_{it} for the electron-hole pair determined by tunneling from valence to conduction band in imaginary time. We have shown that the same tunnel exit x_{it} also governs interband harmonics in a conventional periodic system, improving the agreement of the trajectory traces with the quantum energy-time profile of the harmonics.

Backscattering as introduced here has close analogies in extended atomic systems. However, in the latter it leads only to higher energies in laser-driven photoionization (often termed “above-threshold ionization”), but not to larger high-

order-harmonic cutoffs, since the localized electrons in atomic systems lack the ability for overlap of electron amplitudes at large distances which is possible for the delocalized electrons in quasiperiodic systems. Other sources of breaking the periodicity of solid-state systems, such as impurities, domain walls, or grain boundaries, may also induce backscattering and ensuing effects on HHG. Work in this direction is underway.

C.Y. acknowledges discussion with Lars Bojer Madsen in the early stage of this work.

-
- [1] S. Ghimire, A. D. DiChiara, E. Sistrunk, P. Agostini, L. F. DiMauro, and D. A. Reis, Observation of high-order harmonic generation in a bulk crystal, *Nat. Phys.* **7**, 138 (2011).
- [2] G. Vampa and T. Brabec, Merge of high harmonic generation from gases and solids and its implications for attosecond science, *J. Phys. B* **50**, 083001 (2017).
- [3] S. Ghimire and D. A. Reis, High-harmonic generation from solids, *Nat. Phys.* **15**, 10 (2019).
- [4] C. Yu, S. Jiang, and R. Lu, High-order harmonic generation in solids: A review on recent numerical methods, *Adv. Phys. X* **4**, 1562982 (2019).
- [5] M. Lewenstein, P. Balcou, M. Y. Ivanov, A. L’Huillier, and P. B. Corkum, Theory of high-harmonic generation by low-frequency laser fields, *Phys. Rev. A* **49**, 2117 (1994).
- [6] G. van de Sand and J. M. Rost, Irregular Orbits Generate Higher Harmonics, *Phys. Rev. Lett.* **83**, 524 (1999).
- [7] G. Vampa, C. R. McDonald, G. Orlando, D. D. Klug, P. B. Corkum, and T. Brabec, Theoretical Analysis of High-Harmonic Generation in Solids, *Phys. Rev. Lett.* **113**, 073901 (2014).
- [8] G. Vampa, C. R. McDonald, G. Orlando, P. B. Corkum, and T. Brabec, Semiclassical analysis of high harmonic generation in bulk crystals, *Phys. Rev. B* **91**, 064302 (2015).
- [9] A. M. Parks, G. Ernotte, A. Thorpe, C. R. McDonald, P. B. Corkum, M. Taucer, and T. Brabec, Wannier quasi-classical approach to high harmonic generation in semiconductors, *Optica* **7**, 1764 (2020).
- [10] G. Ndashimiye, S. Ghimire, M. Wu, D. A. Browne, K. J. Schafer, M. B. Gaarde, and D. A. Reis, Solid-state harmonics beyond the atomic limit, *Nature (London)* **534**, 520 (2016).
- [11] N. Tancogne-Dejean, O. D. Mücke, F. X. Kärtner, and A. Rubio, Impact of the Electronic Band Structure in High-Harmonic Generation Spectra of Solids, *Phys. Rev. Lett.* **118**, 087403 (2017).
- [12] D. Bauer and K. K. Hansen, High-Harmonic Generation in Solids with and without Topological Edge States, *Phys. Rev. Lett.* **120**, 177401 (2018).
- [13] T. T. Luu and H. J. Wörner, Measurement of the Berry curvature of solids using high-harmonic spectroscopy, *Nat. Commun.* **9**, 916 (2018).
- [14] R. E. F. Silva, Á. Jiménez-Galán, B. Amorim, O. Smirnova, and M. Ivanov, Topological strong-field physics on sub-laser-cycle timescale, *Nat. Photonics* **13**, 849 (2019).
- [15] T. Ikemachi, Y. Shinohara, T. Sato, J. Yumoto, M. Kuwata-Gonokami, and K. L. Ishikawa, Trajectory analysis of high-order-harmonic generation from periodic crystals, *Phys. Rev. A* **95**, 043416 (2017).
- [16] M. Lein and J. M. Rost, Ultrahigh Harmonics from Laser-Assisted Ion-Atom Collisions, *Phys. Rev. Lett.* **91**, 243901 (2003).
- [17] Z. Wang, A. Camacho Garibay, H. Park, U. Saalmann, P. Agostini, J. M. Rost, and L. F. DiMauro, Universal High-Energy Photoelectron Emission from Nanoclusters Beyond the Atomic Limit, *Phys. Rev. Lett.* **124**, 173201 (2020).
- [18] C. Yu, S. Jiang, T. Wu, G. Yuan, Y. Peng, C. Jin, and R. Lu, Higher harmonic generation from bilayer nanostructures assisted by electron backscattering, *Phys. Rev. B* **102**, 241407(R) (2020).
- [19] K. K. Hansen, T. Deffge, and D. Bauer, High-order harmonic generation in solid slabs beyond the single-active-electron approximation, *Phys. Rev. A* **96**, 053418 (2017).
- [20] See Supplemental Material at <http://link.aps.org/supplemental/10.1103/PhysRevA.105.L041101> for a band-structure picture for a finite chain and a detailed discussion of the laser-driven quiver motion in a Kane band.
- [21] K. K. Hansen, D. Bauer, and L. B. Madsen, Finite-system effects on high-order harmonic generation: From atoms to solids, *Phys. Rev. A* **97**, 043424 (2018).
- [22] C. Yu, H. Irvani, and L. B. Madsen, Crystal-momentum-resolved contributions to multiple plateaus of high-order harmonic generation from band-gap materials, *Phys. Rev. A* **102**, 033105 (2020).
- [23] O. Schubert, M. Hohenleutner, F. Langer, B. Urbanek, C. Lange, U. Huttner, D. Golde, T. Meier, M. Kira, S. W. Koch, and R. Huber, Sub-cycle control of terahertz high-harmonic generation by dynamical Bloch oscillations, *Nat. Photonics* **8**, 119 (2014).
- [24] G. G. Paulus, W. Becker, W. Nicklich, and H. Walther, Rescattering effects in above-threshold ionization: A classical model, *J. Phys. B* **27**, L703 (1994).
- [25] L. Yue and M. B. Gaarde, Imperfect Recollisions in High-Harmonic Generation in Solids, *Phys. Rev. Lett.* **124**, 153204 (2020).
- [26] E. O. Kane, Band structure of indium antimonide, *J. Phys. Chem. Solids* **1**, 249 (1957).
- [27] For our system the parameters $m_*=0.167$ and $k_*=0.2$ lead to $x_q=4.62A_0/\omega_0$ and $N_q=\lambda/165\text{nm}$.

Supplement “High harmonics from backscattering of delocalized electrons”

Chuan Yu, Ulf Saalman and Jan M Rost

1. Band-structure picture for a finite chain

Conceptually, band structures are well-defined for periodic systems. For a finite chain, a multi-well potential with edges is self-consistently determined according to Kohn-Sham DFT, and its corresponding “band structures” can be represented by the k -space distribution of the eigenstates $\{\psi_j(x)\}$ in combination with their corresponding eigenenergies $\{E_j\}$ [1]. It has been demonstrated that a sufficiently large finite system can mimic the band structures of infinite periodic limit [2]. Here we will show that the band-structure picture is also useful for describing the behavior of short chains such as $N = 16$.

Eigenstates with energy $E_j < 0$ are discretized bound states with their wavefunctions basically confined within the chain ($|x| < L/2$) with length $L = Nd$, while eigenstates with energy $E_j > 0$ are in the continuum with their wavefunctions extending outside the system towards infinity in an oscillating manner just as in the atomic and molecular cases. Roughly speaking, the outer-region ($|x| > L/2$) continuum wavefunctions lead to the free-space parabola $E = k^2/2$, while the inner-region ($|x| < L/2$) part contains the signature of band structures determined by the multi-well potential. For a better comparison with the periodic-system band structures, here we exclude the free-space parabola by Fourier transforming only the inner-region part of eigenfunctions $\psi_j(x)$,

$$\tilde{\psi}_j(k) = \int dx w(x) \psi_j(x) \exp(-ikx), \quad (\text{S1})$$

with the smooth window function

$$w(x) = \begin{cases} 1, & |x| < L/2 \\ \cos^2\left(\frac{\pi}{d}(|x| - L/2)\right), & L/2 \leq |x| \leq L/2 + d/2 \\ 0, & |x| > L/2 + d/2 \end{cases}. \quad (\text{S2})$$

For our purpose of visualizing the “band structures” of a finite chain, this treatment causes negligible modifications to the bound-state wavefunctions and it approximately extracts the energy dispersion within the chain.

Figure S1 shows the k -space distribution $\{|\tilde{\psi}_j(k)|^2\}$ at the corresponding energy levels $\{E_j\}$ for a short chain of $N = 16$. This plot includes eigenstates in \mathcal{V}_2 , \mathcal{C}_1 and \mathcal{C}_2 bands, which are relevant for the HHG processes discussed in this work. Motivated by the good agreement between the energy dispersion shown as the main peaks of $\{|\tilde{\psi}_j(k)|^2\}$ and the periodic-system band structures, in this work we illustrate the backscattering dynamics in finite chains using the band-structure picture.

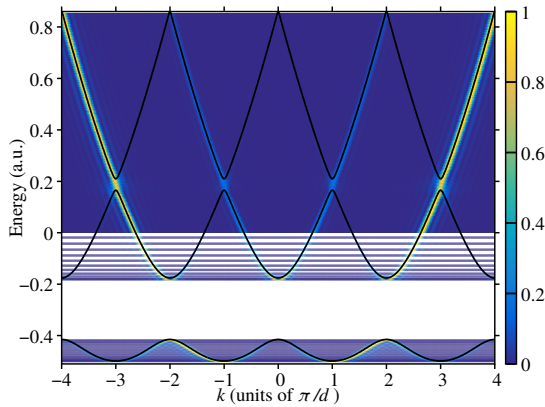


Figure S1: The k -space distribution $\{|\tilde{\psi}_j(k)|^2\}$, normalized such that the highest peak is equal to 1, at the corresponding energy levels $\{E_j\}$ for a short chain of $N = 16$. The periodic-system band structures are shown in the repeated zone scheme as black lines. The k values corresponding to the highest peaks of $\{|\tilde{\psi}_j(k)|^2\}$ agree well with the periodic-system band structures (in the extended zone scheme).

2. Laser-driven quiver motion in a Kane band

In the Kane model [3] the band structure is approximated up to a constant by

$$E(k) = E_b \sqrt{1 + k^2/(m_* E_b)}, \quad (\text{S3})$$

with E_b a characteristic band energy and m_* the effective mass. This model represents the real band structure extremely well, as can be seen in Fig. S2. The group velocity in this band reads

$$\frac{d}{dk} E(k) = \frac{k/m_*}{\sqrt{1 + k^2/k_*^2}} \quad \text{with } k_* \equiv \sqrt{m_* E_b}, \quad (\text{S4})$$

which shows that, particularly if k is larger than the characteristic band momentum k_* , the free-particle velocity k/m_* , given by the numerator, is modified such that it saturates at a maximal value of k_*/m_* . Note that k_* characterizes the point where the band dispersion changes from parabolic to quasi-linear behavior.

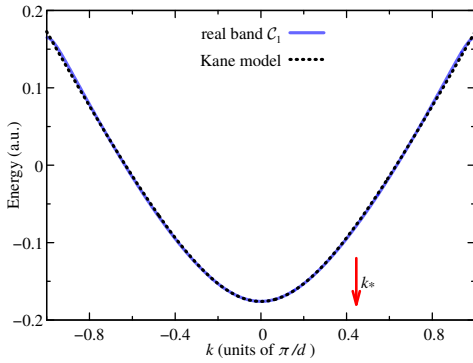


Figure S2: The Kane model (S3) in comparison to the real structure of the 1st conduction band. The model (black dotted line) perfectly matches the real band (blue solid line) except from tiny deviations at the Brillouin-zone boundaries. The characteristic band momentum k_* is shown by the red arrow.

Assuming that k follows the oscillating vector potential $A(t) = A_0 \sin(\omega t)$, one can calculate the quiver position of a particle starting at $x(t_0) = 0$ by

$$x(t) = \frac{A_0/\omega}{m_*} \int_{\varphi_0}^{\varphi} d\varphi' \frac{\sin \varphi' - \sin \varphi_0}{\sqrt{1 + a^2 [\sin \varphi' - \sin \varphi_0]^2}}, \quad (\text{S5})$$

where the dimensionless $a \equiv A_0/k_*$ is the “normalized” vector potential. The integration limits are $\varphi_0 = \omega t_0$ and $\varphi = \omega t$, respectively. Apparently the conventional (free-space) quiver motion and thus its amplitude are modified. The modification of the amplitude A_0/ω are caused by both the effective mass m_* and the integral over φ' .

There is no simple analytical expression for the integral in (S5) for arbitrary initial phase φ_0 . Nevertheless, for the special case of $\varphi_0 = 0$ corresponding to a laser-field extremum, the quiver amplitude is maximal, and the integral in (S5) leads to a simple analytical expression, namely $x_q = \xi_a A_0/m_* \omega$ with $\xi_a \equiv \arctan(a)/a$. The prefactor ξ_a reduces the quiver amplitude and takes the values $\xi_0 = 1$, $\xi_1 = \pi/4$ and $\xi_{a \rightarrow \infty} = \pi/2a$, respectively. For the chains considered in this work, the parameters $E_b = 0.239$ and $m_* = 0.167$ result for $A_0 = 0.21$ in $a = 1.05$. Due to the small effective mass m_* , the quiver amplitude of the conduction-band electron is much larger than the free-electron quiver radius A_0/ω in the atomic case. This is only weakly compensated by the prefactor $\xi_{1.05} = 0.77$ in the situation considered here.

- [1] K. K. Hansen, T. Deffge, and D. Bauer, *High-order harmonic generation in solid slabs beyond the single-active-electron approximation*. Phys. Rev. A **96**, 053418 (2017).
- [2] C. Yu, H. Irvani, and L. B. Madsen, *Crystal-momentum-resolved contributions to multiple plateaus of high-order harmonic generation from band-gap materials*. Phys. Rev. A **102**, 033105 (2020).
- [3] E. O. Kane, *Band structure of indium antimonide*. J. Phys. Chem. Solids **1**, 249 (1957).